ADVANCED MATERIALS
www.advmat.de

Non-Hermitian Selective Thermal Emitters using Metal–Semiconductor Hybrid Resonators

*Chloe F. Doiron and Gururaj V. Naik**

All open systems that exchange energy with their environment are non-Hermitian. Thermal emitters are open systems that can benefit from the rich set of physical phenomena enabled by their non-Hermitian description. Using phase, symmetry, chirality, and topology, thermal radiation from hot surfaces can be unconventionally engineered to generate light with new states. Such thermal emitters are necessary for a wide variety of applications in sensing and energy conversion. Here, a non-Hermitian selective thermal emitter is experimentally demonstrated, which exhibits passive *PT*-symmetry in thermal emission at 700 °C. Furthermore, the effect of internal phase of the oscillator system on far-field thermal radiation is experimentally demonstrated. The ability to tune the oscillator phase provides new pathways for both engineering and controlling selective thermal emitters for applications in sensing and energy conversion.

Thermal light sources generate light directly from heat making them useful for a wide variety of applications in sensing[1] and energy conversion.[2–5] Thermal emitters require optical losses to emit thermal radiation, through which they exchange energy with the environment, making them open systems.[6] Open systems differ from closed systems in that they cannot be described by Hermitian physics as their eigenvalue spectrum is no longer required to be real. Hence, all thermal emitters are non-Hermitian systems. Non-Hermitian systems may provide novel design tools for thermal emitters such as symmetry,[7,8] topology,[9,10] and phase.[11] Non-Hermitian systems comprising a nearly closed subsystem coupled with a nearly open subsystem are interesting. Such systems possess parity-time symmetry (*PT*-symmetry) and exhibit an optical phase transition between weak and strong coupling regimes[12,13] at the exceptional point. At the exceptional point, the Hilbert space of the system becomes severely skewed[14,15] and as a result, the system becomes extremely sensitive to small perturbations. Furthermore, an exceptional point has topological properties such as chirality[14] and unidirectional energy transfer between the eigenmodes when encircling a path.[16,17] Thus, the physics of non-Hermitian systems is fascinatingly different from Hermitian systems and therefore its exploration in the context of thermal emitters can provide new methods to design and build thermal emitters with extreme spatial and spectral properties.

Because thermal emitters always require optical losses, coupling them with lossless resonators can result in systems displaying passive *PT*-symmetry. A simple mathematical description of this system is as a pair of coupled oscillators with extreme asymmetry in optical losses as described by the Hamiltonian in Equation (1)

$$\hat{H} = \begin{pmatrix} \omega_1 + \gamma_1 \cdot i & \kappa \\ \kappa & \omega_2 + \gamma_2 \cdot i \end{pmatrix}, \text{with } \gamma_1 \approx 0 \text{ and } \omega_1 \approx \omega_2 \quad (1)$$

The eigenstates of this passive *PT*-symmetric device can be controlled by varying either the coupling between resonators κ or the damping of the lossy resonator γ_2. Consequently, the thermal emission from this system can be engineered by the same parameters which makes non-Hermitian systems an exciting platform for designing selective thermal emitters.

Plasmonic nanostructures are an obvious choice for a lossy resonator. The optical properties of metals, commonly used in thermal emitters, degrade significantly at high temperatures making a plasmonic resonator a nearly open subsystem.[1,18–21] On the other hand, common semiconductors in the sub-bandgap region (1500–6500 cm^{-1}) have negligible optical losses and remain almost lossless even at elevated temperatures up to 1000 °C.[2,22] Because of this, sub-micrometer semiconductor structures can form high-Q resonators that can be approximated as nearly closed subsystems. Thus, a coupled plasmonic-semiconductor resonator system makes an ideal platform for a passive *PT*-symmetric thermal emitter.

We implemented this system by fabricating cylindrical silicon resonators on a MgF_2 dielectric spacer layer on a tungsten substrate as shown in the schematic of **Figure 1**a. The silicon disk is the lossless resonator while the surface plasmon-polaritons excited on tungsten is the lossy resonator as depicted in Figure 1c. The coupling between the two resonators is controlled by the thickness of the MgF_2 spacer layer which is varied in our experiments. The simple Hamiltonian shown in Equation (1) can describe our system

C. F. Doiron, Prof. G. V. Naik
Department of Electrical and Computer Engineering
Rice University
Houston, TX 77005, USA
E-mail: guru@rice.edu
C. F. Doiron
Applied Physics Graduate Program
Smalley-Curl Institute
Rice University
Houston, TX 77005, USA
The ORCID identification number(s) for the author(s) of this article can be found under https://doi.org/10.1002/adma.201904154.

DOI: 10.1002/adma.201904154

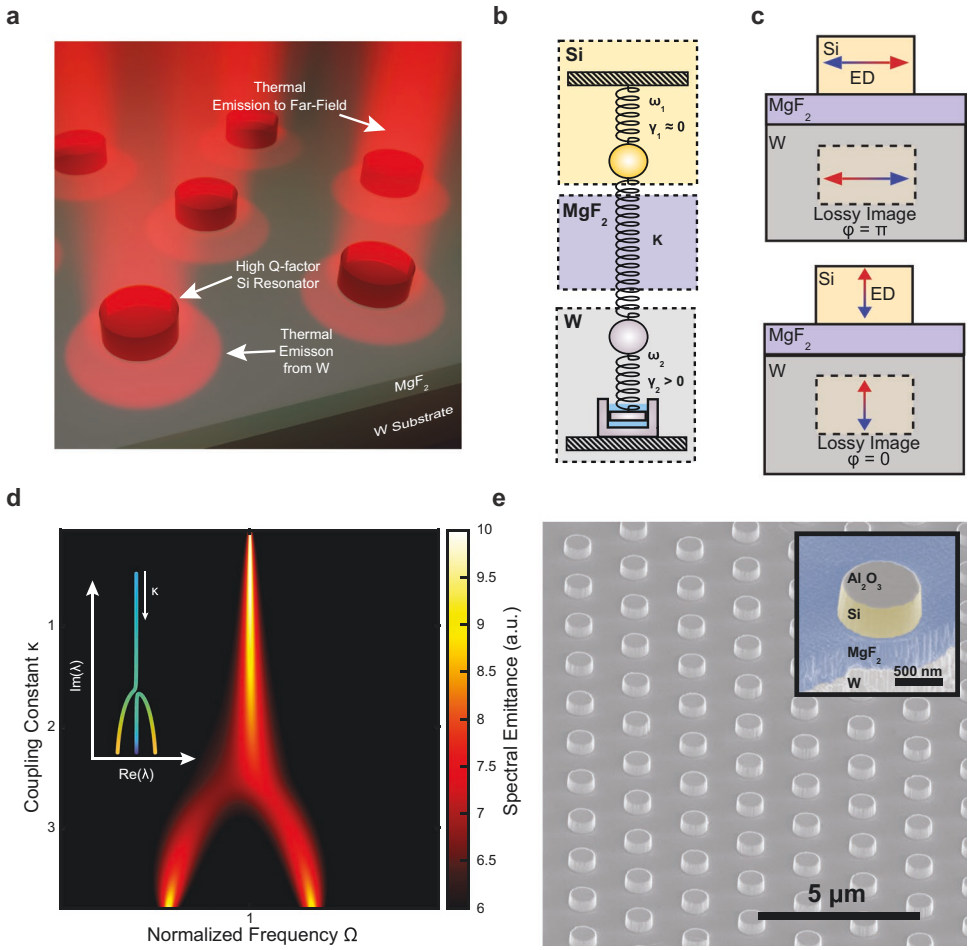

Figure 1. a) Representation of the semiconductor–insulator–metal structure forming a coupled photonic and plasmonic resonator system. b) Diagram showing classical oscillator analogue of coupled resonator system. c) Induced lossy plasmonic resonators with electric and magnetic mirrors allowing the phase offset to be tuned. d) Calculated thermal emission spectra from lumped circuit model using a coupled lossy capacitive and inductive resonator system showing *PT*-symmetry. The frequency is normalized to the resonance frequency in the broken *PT*-symmetry phase. Inset: Eigenvalues for the coupled resonator system as a function of coupling showing a branch point. e) Scanning electron microscopy (SEM) image of fabricated device. Inset: False-color, cross-section image of fabricated structure.

by considering the interaction of the silicon resonator with its image in the tungsten ground plane. The losses in tungsten make the image resonator lossy as depicted in Figure 1c. Through the combination of spatial inversion and loss asymmetry, the system satisfies the conditions for passive *PT*-symmetry.[23]

A lumped circuit element model, described in Note S1 in the Supporting Information, for our thermal emitter system predicts an optical phase transition at the exceptional point and the resultant thermal radiation spectrum also shows the same behavior as seen in Figure 1d. It is important to note that *PT*-symmetric behavior is observed when the oscillators are in- or out-of-phase with each other as shown in Figure S1b in the Supporting Information. Strong thermal emission occurs in both the *PT*-symmetric and broken *PT*-symmetry phases, but not at the exceptional point. This occurs because in both of these optical phases small imaginary components of eigenvalues can be achieved, as seen in the inset, allowing the system to more efficiently out-couple thermal radiation.[24,25] At the exceptional point, thermal emission is reduced because of the relatively large imaginary components of eigenvalues.

The implementation of our non-Hermitian thermal emitter requires a periodic array of silicon disks coupled via MgF_2 spacer to tungsten. Isolated silicon resonators were not capable of displaying passive *PT*-symmetry as shown in Figure S2 in the Supporting Information. A scanning electron microscopy (SEM) image of a fabricated sample is shown in Figure 1e. The silicon disks are 800 nm in diameter and 400 nm tall making a hexagonal lattice with a nearest neighbor separation of 2 µm. The periodic array of silicon disks forms a metasurface that suppresses the radiative damping of a single silicon resonator. In order to preserve the non-Hermitian behavior of the local resonance of an individual silicon disk, we design a Friedrich–Wintgen quasi bound state in the continuum (BIC). The quasi-BIC design allows treating the silicon disk array as a collection of individual resonators coupled to the plasmonic substrate.

The full wave simulations of far-field thermal emission in the direction normal to our non-Hermitian device is shown in **Figure 2**a for various MgF_2 thicknesses. When no MgF_2 is present, two strong peaks are observed at 2900 and 4700 cm^{-1}. As the MgF_2 thickness increases to 180 nm, these two modes

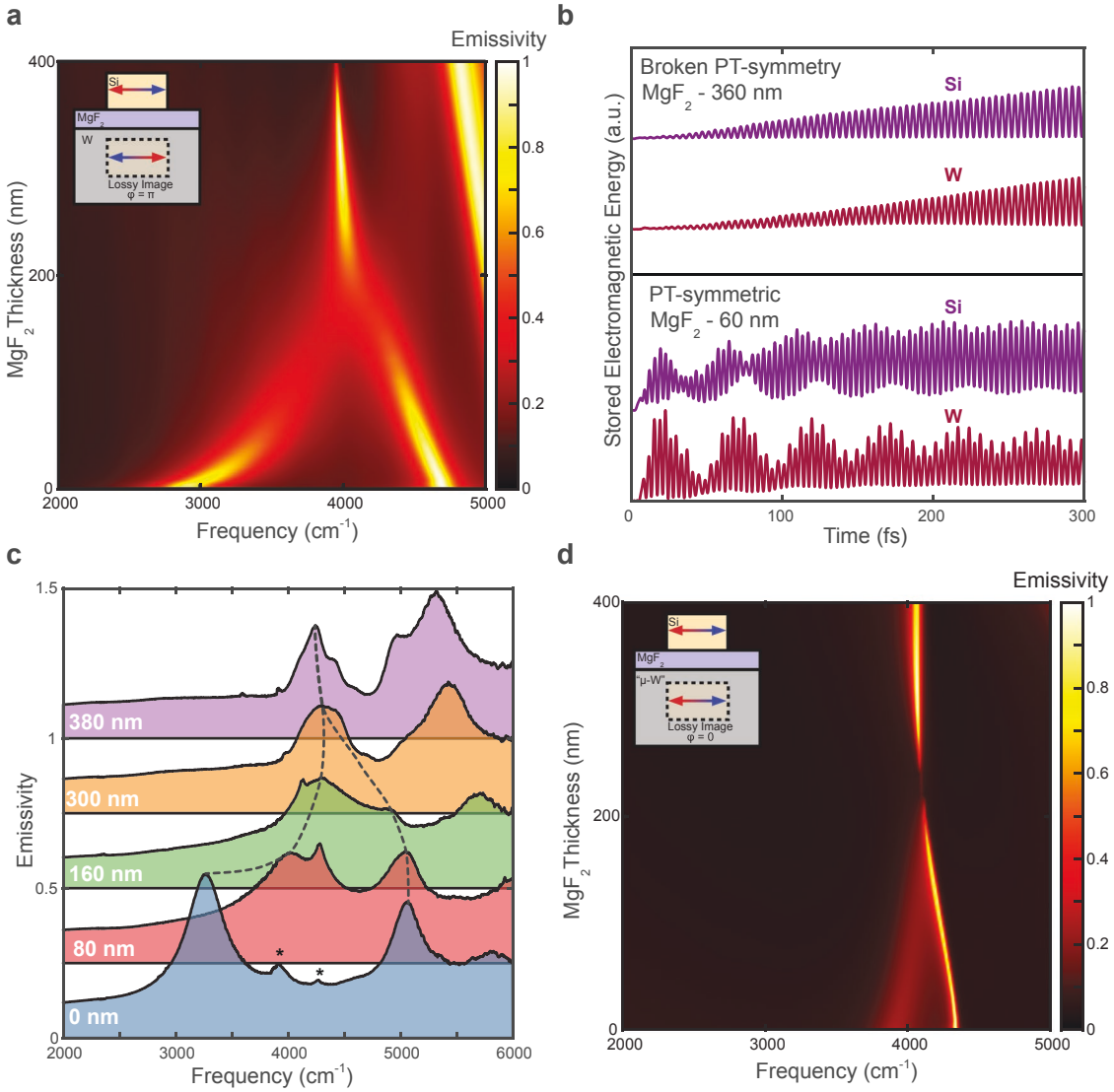

Figure 2. a) Simulated thermal emission spectra of coupled semiconductor–insulator–metal system showing *PT*-symmetry. b) Simulated energy densities of the silicon and tungsten resonators. Rabi oscillations occur in the *PT*-symmetric phase. These oscillations are no longer present when the system is in the broken *PT*-symmetry phase. c) Experimental thermal emission measurements for several MgF_2 thicknesses. The vertical modes are denoted with an asterisk. d) Full-wave simulations of *PT*-symmetric behavior when a lossy magnetic mirror is used as the substrate. The in-phase image dipole, as in the case of a vertical dipole, exhibits a distinctly different *PT*-symmetric behavior.

merge together at a branch point occurring near the exceptional point. Increasing the MgF_2 spacing even further to 320 nm, *PT*-symmetry is broken and only a single mode remains at 4000 cm^{-1}. To determine if the coupled resonator system undergoes an optical phase transition, the most robust method is to look at the energy exchange between the oscillators as a function of time.[26] We calculated the stored electromagnetic energy as a function of time in the silicon and tungsten resonators when the system is driven by dipoles in the photonic resonators. A complete description of the calculation method is provided in Note S4 in the Supporting Information. In the *PT*-symmetric phase, the oscillators are strongly coupled and exhibit energy exchange due to Rabi oscillations. In contrast, a monotonic increase in energy is observed in the broken *PT*-symmetry phase.

The measured thermal emission spectra are shown in Figure 2c at an operating temperature of 700 °C. As expected from simulations, we observed two prominent peaks at 3270 and 5050 cm^{-1} when there was no MgF_2 layer. When the MgF_2 layer thickness is increased to 300 nm, both of these prominent peaks merge together as predicted by both the analytical model and full-wave simulations. When the dielectric layer thickness is increased even further, the system transitions to the broken *PT*-symmetry phase where the eigenvalues determining peak emission diverge in the imaginary part, but have the same real part. This causes the *Q*-factor of the thermal emission peak to increase to 37 while maintaining a nearly constant peak emissivity. From these measurements, we can observe that by tuning the MgF_2 spacer thickness, we can tune the coupled resonator system from the *PT*-symmetric to the broken *PT*-symmetry phase.

The thermal emission spectra in Figure 2c were collected in the normal direction using an objective with a maximum acceptance angle of 4.6°. The off normal collection probes the vertical modes supported in the sample observed in Figure 2c. The two peaks at 3930 and 4270 cm^{-1} for the sample with no MgF_2 spacer are from the vertical mode. Similar to the horizontal mode, the vertical mode is localized and exhibits passive *PT*-symmetry via interaction with its image dipole. Unlike the horizontal mode with an out-of-phase image, the vertical mode has an in-phase image, which results in larger damping. As a result, the *PT*-symmetric feature exhibited by the vertical mode is distinctly different from the horizontal mode. Figure 2d highlights this point by plotting the expected *PT*-symmetric behavior when the tungsten electric mirror is replaced by an equivalent magnetic mirror. The magnetic mirror creates an in-phase image of the horizontal dipole resulting in larger damping. Hence, the splitting between the modes in the *PT*-symmetric phase is smaller. Also, the exceptional point occurs at a smaller spacer thickness (larger coupling constant). This same behavior can be seen in the experimental measurements in Figure 2c. More details on the vertical mode and off-normal simulations are provided in Note S7 in the Supporting Information. These results demonstrate that internal phase of the coupled oscillators is a powerful tool to tune far-field thermal radiation. Through proper design of the phase profile of coupled resonators, thermal emission can exhibit super-radiance (in-phase oscillators) and subradiance (out-of-phase oscillators) leading to sublinear and superlinear scaling, respectively.[8,27] With further study, *PT*-symmetric super-radiance or subradiance may be possible by engineering the internal phase of many such coupled oscillators.

The mode localization required in our device is enabled by the quasi-BIC mode supported by the silicon resonator array. The quasi-BIC mode originates from balancing the damping rates of the electric and magnetic dipolar modes of the silicon resonator to the continuum. This feature can be observed in the simulated total reflectance spectra at normal incidence of the resonator array with different diameters of silicon disks shown in **Figure 3**a. Tuning the diameter of the silicon disks results in an avoided crossing of electric and magnetic dipolar modes. The avoided crossing is difficult to observe due to high radiative damping. However, the interaction between the two modes results in a quasi-BIC mode that manifests in a Fano line shape. Silicon disk diameter of 950 nm exhibits such Fano line shape indicating the avoided crossing behavior.[28,29] The quasi-BIC mode in our metasurface results in flat bands at the Γ-point

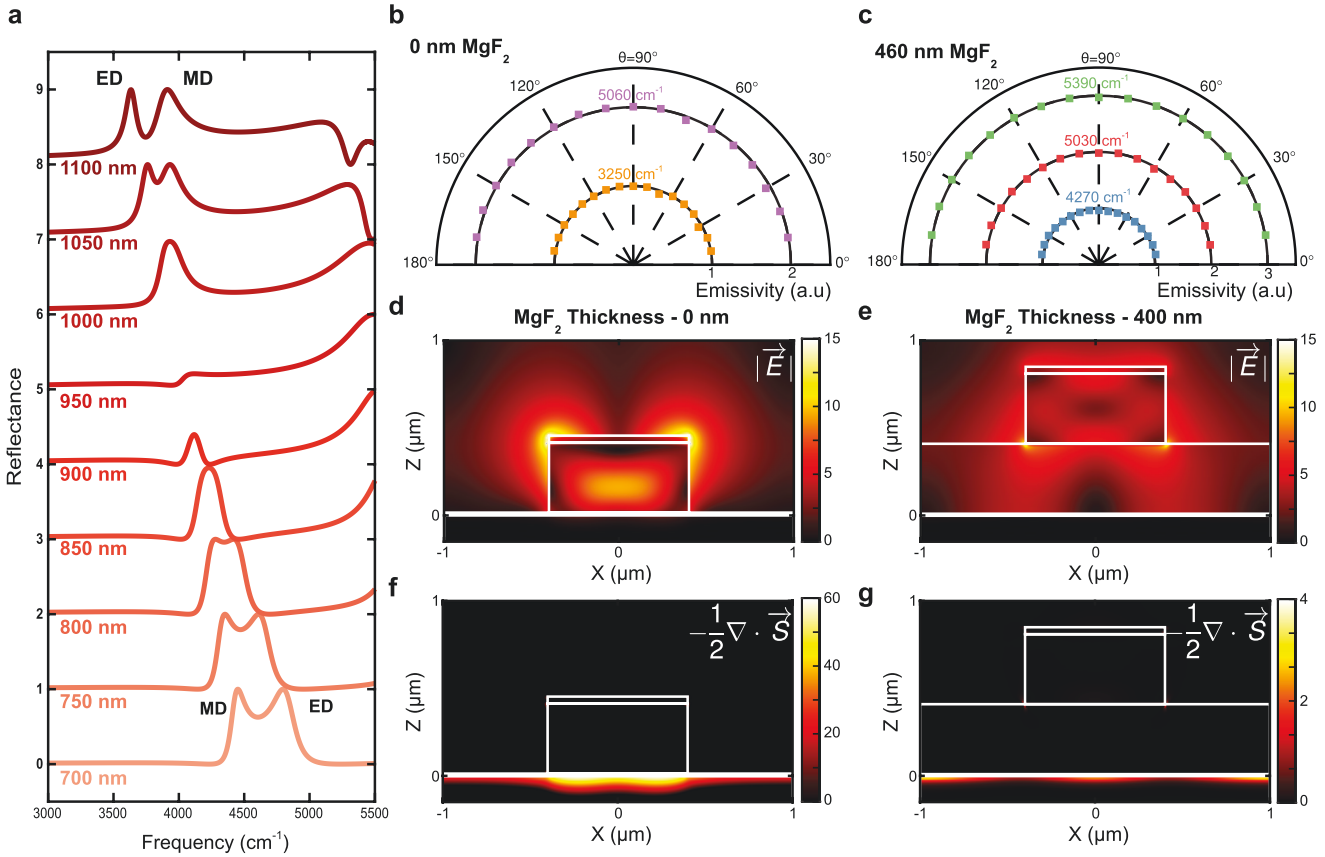

Figure 3. a) Full-wave simulations of total reflectance at normal incidence on a hexagonal lattice of cylindrical silicon photonic resonators with 2 μm periodicity and diameters from 700 to 1100 nm showing the presence of electric (ED) and magnetic (MD) dipole modes. When the resonances nearly cross, a Friedrich–Wintgen quasi bound state in the continuum (BIC) occurs. b,c) Experimental polarization resolved thermal emission measurements for samples in *PT*-symmetric (0 nm MgF_2) (b) and broken *PT*-symmetry (460 nm MgF_2) (c) phases. The independence of emissivity from polarization demonstrates the modes are localized. d,e) Magnitude of electric field for *PT*-symmetric (d) and broken *PT*-symmetry (e) phases. f,g) The divergence of Poynting vector in the cases of *PT*-symmetric (f) and broken *PT*-symmetry (g) phases shows that the source of thermal emission is the lossy plasmonic resonance.

in the band structure shown in Figure S3 in the Supporting Information. As a result, the thermal emission from quasi-BIC modes should be independent of the collection polarization at near normal emittance. Figure 3b,c plots the measured thermal emission intensity for near normal emittance for various polarizations with respect to the hexagonal lattice. The modes in the *PT*-symmetric and broken *PT*-symmetry phases show no polarization dependence indicating that emission originates from a localized resonance. Additionally, higher order modes also display no polarization dependence due to the localization of resonances to individual silicon disks.

The energy storage behavior in our device is very different in the two optical phases. The simulated field profiles of our device with no MgF_2 (*PT*-symmetric) and 400 nm of MgF_2 spacer (broken *PT*-symmetry) are shown in Figure 3d–g. In the *PT*-symmetric phase, the photonic and plasmonic resonators are strongly coupled leading to energy exchange, through Rabi oscillations, and mode hybridization. In contrast, the magnitude of electric field distribution shows strong energy storage behavior in the silicon resonator in the broken *PT*-symmetry phase. This results in the silicon resonator storing a majority of the total stored electromagnetic energy in the system. However, from the divergence of the Poynting vector, it is clear that more than 98% of the thermal emission originates from the tungsten substrate in both optical phases. Combining the experimental results together with these field plots demonstrate that our device has localized coupled resonators with passive *PT*-symmetry.

The vertical and horizontal modes observed in our device individually exhibit *PT*-symmetry as seen in Figure 2c and Figure S8 in the Supporting Information. However, by increasing the collection angle to just 10°, we observe that the two modes couple. The coupling between the modes and their images (κ) and that between the horizontal and vertical modes (κ_{hv}) results in a 4D Hamiltonian presented in Equation (S10) in the Supporting Information. **Figure 4**a shows the expected evolution of thermal emission spectrum for a system of two passive *PT*-symmetric systems coupled together. Here, we fix κ_{hv} at 0.4 and vary κ to study the effect of spacer thickness. The four modes together exhibit *PT*-symmetric behavior and optical phase transitions at two clear branch points. Compared to the case when there is no coupling between the horizontal and vertical modes (normal emittance case), κ_{hv} = 0.4 results in relatively small shifts to the modes in the *PT*-symmetric phase while modes in the broken *PT*-symmetry phase experience large shifts.

Measured thermal emission from samples with MgF_2 thicknesses ranging from 0 to 380 nm are presented in Figure 4b. When no MgF_2 is present, four strong peaks can be observed. Increasing the spacer thickness from 300 to 380 nm, peak positions remain unchanged indicating that the system is in the broken *PT*-symmetry phase. As expected, when the thickness of the MgF_2 spacer layer is 380 nm, the modes span a frequency range of almost 700 cm^{-1} compared to just 300 cm^{-1} for normal emittance measurements. In addition to demonstrating the effect of internal phase, these experimental measurements demonstrate coupling between the horizontal and vertical passive *PT*-symmetric resonances that could be exploited for achieving higher order exceptional points.[30,31]

In summary, we demonstrated that a non-Hermitian description of thermal emitters opens new avenues to engineer thermal radiation. We built a passive *PT*-symmetric thermal emitter using a quasi-BIC mode of a silicon disk metasurface coupled to the plasmonic mode of a tungsten substrate. We showed that our device exhibits two optical phases with very different energy storage profiles. In the weak coupling regime, we showed that the thermal emission primarily originates from lossy tungsten, but is efficiently stored in the nearly lossless silicon resonator. Furthermore, we demonstrated that the internal phase of the coupled oscillators presents a new tool to tailor thermal radiation. This demonstration confirms that non-Hermitian physics may be applied to fluctuational systems and presents unorthodox methods to engineer thermal radiation.

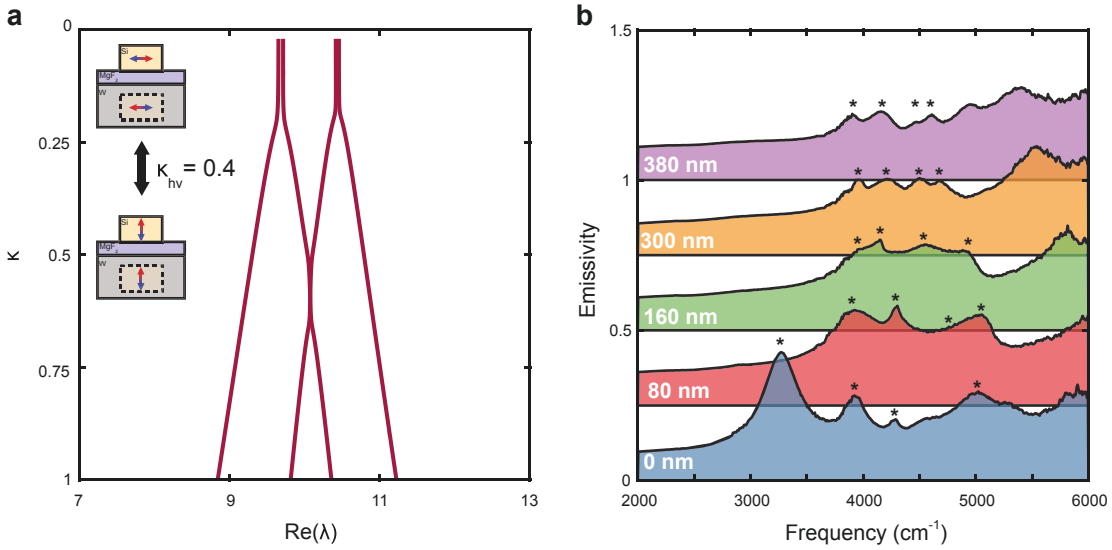

Figure 4. a) Real component of eigenvalues for the case of two sets of *PT*-symmetric oscillators coupled to each other with κ_{hv} = 0.4. b) Experimental measurements of emissivity measured with the sample tilted 10° toward the K-point for several thicknesses of MgF_2. As the MgF_2 thickness is increased, we see that the four distinct modes, denoted with *, merge into two groups of two modes spanning almost 700 cm^{-1}.

Experimental Section

Simulation Methods: Full-wave electromagnetic simulations were performed using finite-difference time-domain using a commercial software package (Lumerical, FDTD). High-temperature optical properties for tungsten were obtained from experimental measurements.[19] The high temperature optical properties of silicon were calculated using semiphysical models.[22] The optical properties of MgF_2 were assumed to be independent of temperature. To investigate the internal phase on the non-Hermitian selective thermal emitter, the silicon resonator array was simulated on top of an artificial magnetic mirror coated with MgF_2. The optical constants of an artificial magnetic mirror can be created by fitting the optical properties of W with a single Lorentz oscillator. For the magnetic mirror, the Lorentz oscillator was used to calculate the magnetic permeability, while the relative permittivity was 1.

Fabrication Process: The non-Hermitian thermal emitters were fabricated using polished W substrates (MTI, W-101005S2-P). First, layers of Al_2O_3 (10 nm), MgF_2 (0–460 nm), and Si (400 nm) were deposited using e-beam evaporation on the W substrate. The thin layer of Al_2O_3 served two purposes, first it acted as a diffusion barrier between tungsten and silicon preventing the formation of tungsten-silicide. Additionally, the film was an adhesion layer for the MgF_2 dielectric spacer. Without this layer, the MgF_2 films were found to delaminate during nanofabrication. Next, a 45 nm thick Al_2O_3 etch mask was patterned using a standard e-beam lithography (JEOL, JBX5500FS) liftoff process. Silicon nanopillars were formed using a reactive ion etch (Oxford, Plasmalab System 100/ICP 180) with a mixture of C_4F_8 and SF_6 with flow rates of 57 and 33 sccm, respectively. The capacitively and inductively coupled RF powers were maintained at 20 and 1200 W, respectively.

Experimental Characterization Process: All thermal emission measurements were carried out using a Fourier-transform infrared spectrometer (Thermo Fisher Scientific, iS50R) with samples heated up in vacuum stage (Microptik, MHS1200-V/G) with a PID temperature controlled heater element. The vacuum pressure was maintained below 5×10^{-6} Torr. Optical access to the sample was through a ZnSe window and thermal radiation was collected using a ZnSe refractive objective with NA 0.08 (Edmund Optics, 88-448). All thermal emission measurements used a solid tungsten substrate (10 mm × 10 mm × 0.5 mm) with surface roughness <3 nm as an emissivity reference. Because of the low surface roughness, diffuse reflectance was negligible allowing the absorption spectrum of the tungsten substrate to be characterized through specular reflectance measurements. Specular reflectance measurements performed at 700 °C were used to determine absorption and therefore emissivity through Kirchhoff's law of thermal radiation.

Supporting Information

Supporting Information is available from the Wiley Online Library or from the author.

Acknowledgements

This material is based upon work supported by the National Science Foundation under Grant No. ECCS-1935446.

Conflict of Interest

The authors declare no conflict of interest.

Keywords

infrared sources, metamaterials, non-Hermitian photonics, *PT*-symmetric photonics, thermal emitters

Received: June 30, 2019
Revised: August 27, 2019
Published online:

[1] A. Lochbaum, Y. Fedoryshyn, A. Dorodnyy, U. Koch, C. Hafner, J. Leuthold, *ACS Photonics* **2017**, *4*, 1371.
[2] T. Asano, M. Suemitsu, K. Hashimoto, M. De Zoysa, T. Shibahara, T. Tsutsumi, S. Noda, *Sci. Adv.* **2016**, *2*, e1600499.
[3] P. N. Dyachenko, S. Molesky, A. Y. Petrov, M. Störmer, T. Krekeler, S. Lang, M. Ritter, Z. Jacob, M. Eich, *Nat. Commun.* **2016**, *7*, 11809.
[4] J. K. Tong, W.-C. Hsu, Y. Huang, S. V. Boriskina, G. Chen, *Sci. Rep.* **2015**, *5*, 10661.
[5] B. J. O'Regan, Y. Wang, T. F. Krauss, *Sci. Rep.* **2015**, *5*, 13415.
[6] C. M. Bender, *Rep. Prog. Phys.* **2007**, *70*, 947.
[7] H. Hodaei, M.-A. Miri, M. Heinrich, D. N. Christodoulides, M. Khajavikhan, *Science* **2014**, *346*, 975.
[8] S. Yi, M. Zhou, Z. Yu, P. Fan, N. Behdad, D. Lin, K. X. Wang, S. Fan, M. Brongersma, *Nat. Nanotechnol.* **2018**, *13*, 1143.
[9] G. Harari, M. A. Bandres, Y. Lumer, M. C. Rechtsman, Y. D. Chong, M. Khajavikhan, D. N. Christodoulides, M. Segev, *Science* **2018**, *359*, eaar4003.
[10] M. A. Bandres, S. Wittek, G. Harari, M. Parto, J. Ren, M. Segev, D. N. Christodoulides, M. Khajavikhan, *Science* **2018**, *359*, eaar4005.
[11] Y. Choi, C. Hahn, J. W. Yoon, S. H. Song, P. Berini, *Nat. Commun.* **2017**, *8*, 14154.
[12] C. M. Bender, M. Gianfreda, Ş. K. Özdemir, B. Peng, L. Yang, *Phys. Rev. A* **2013**, *88*, 062111.
[13] M. F. Limonov, M. V. Rybin, A. N. Poddubny, Y. S. Kivshar, *Nat. Photonics* **2017**, *11*, 543.
[14] B. Peng, Ş. K. Özdemir, M. Liertzer, W. Chen, J. Kramer, H. Yilmaz, J. Wiersig, S. Rotter, L. Yang, *Proc. Natl. Acad. Sci. U SA* **2016**, *113*, 6845.
[15] W. Chen, Ş. K. Özdemir, G. Zhao, J. Wiersig, L. Yang, *Nature* **2017**, *548*, 192.
[16] H. Xu, D. Mason, L. Jiang, J. G. Harris, *Nature* **2016**, *537*, 80.
[17] Q. Zhong, M. Khajavikhan, D. N. Christodoulides, R. El-Ganainy, *Nat. Commun.* **2018**, *9*, 4808.
[18] J. A. Briggs, G. V. Naik, Y. Zhao, T. A. Petach, K. Sahasrabuddhe, D. Goldhaber-Gordon, N. A. Melosh, J. A. Dionne, *Appl. Phys. Lett.* **2017**, *110*, 101901.
[19] M. Minissale, C. Pardanaud, R. Bisson, L. Gallais, *J. Phys. D: Appl. Phys.* **2017**, *50*, 455601.
[20] T. D. Dao, K. Chen, S. Ishii, A. Ohi, T. Nabatame, M. Kitajima, T. Nagao, *ACS Photonics* **2015**, *2*, 964.
[21] V. W. Brar, M. C. Sherrott, M. S. Jang, S. Kim, L. Kim, M. Choi, L. A. Sweatlock, H. A. Atwater, *Nat. Commun.* **2015**, *6*, 7032.
[22] C. F. Doiron, G. V. Naik, *J. Opt.* **2018**, *20*, 084001.
[23] C. E. Rüter, K. G. Makris, R. El-Ganainy, D. N. Christodoulides, M. Segev, D. Kip, *Nat. Phys.* **2010**, *6*, 192.
[24] H. A. Haus, *Waves and Fields in Optoelectronics*, Prentice-Hall, Englewood Cliffs, NJ, USA **1984**.
[25] S. Zanotto, A. Tredicucci, *Sci. Rep.* **2016**, *6*, 24592.
[26] C. M. Bender, B. K. Berntson, D. Parker, E. Samuel, *Am. J. Phys.* **2013**, *81*, 173.
[27] M. Zhou, S. Yi, T. S. Luk, Q. Gan, S. Fan, Z. Yu, *Phys. Rev. B* **2015**, *92*, 024302.
[28] C. W. Hsu, B. Zhen, A. D. Stone, J. D. Joannopoulos, M. Soljačić, *Nat. Rev. Mater.* **2016**, *1*, 16048.
[29] T. Lepetit, E. Akmansoy, J. P. Ganne, J. M. Lourtioz, *Phys. Rev. B* **2010**, *82*, 195307.
[30] A. Kodigala, T. Lepetit, B. Kanté, *Phys. Rev. B* **2016**, *94*, 201103.
[31] H. Hodaei, A. U. Hassan, S. Wittek, H. Garcia-Gracia, R. El-Ganainy, D. N. Christodoulides, M. Khajavikhan, *Nature* **2017**, *548*, 187.